

Numerical Investigation of Turbulent Buoyant Cavity Flow Using Large Eddy Simulation

S.-H. Peng and L. Davidson

*Department of Thermo and Fluid Dynamics, Chalmers University of Technology,
SE-412 96 Gothenburg, Sweden*

Abstract — A buoyant flow in a cavity with two differentially heated side walls was numerically investigated by means of large eddy simulation. The flow is characterized by stable thermal stratification and relatively low turbulence level ($Ra = 1.58 \times 10^9$). The result for the mean flow quantities shows good agreement with the experiment, while there exist some discrepancies in the prediction of turbulence statistics. In the viscous/conductive sublayer of the boundary layer close to the heated/cooled vertical walls, the flow tends to form coherent structures with low- and high-speed streaks, which do not however emerge in the flow along the horizontal top and bottom walls. Such a flow feature requires sufficient spanwise resolution even when a homogeneous flow is assumed in this direction.

1. Introduction

Large eddy simulation (LES) is increasingly used for simulating turbulent buoyant flows. Various subgrid scale (SGS) models have been applied and show encouraging performance for which comparisons have usually been subjected to the well known Rayleigh-Bénard (RB) convection arising between two horizontal infinite planes. The RB convection in the turbulent regime is characterized by two distinct scales of motion: large-scale coherent structure associated with plumes, thermals and convective cells, and the turbulence generated mainly in the wall boundary layer and carried away by the large scale structure. Such a large-structure flow feature makes the RB convection particularly suitable to the use of LES, indicating the reason for the fairly large degree of success of LES applied to this type of flows.

Unlike the RB convection, turbulent natural convection occurring in a confined cavity with differentially heated side walls is often characterized by the formation of boundary layers along the enclosure surfaces with an encircled recirculating core region. The boundary layer interacts with the wall shear as well as with the core region, which is usually nearly stationary. A large span of scales interacts with each other, introducing difficulties in the numerical resolution [1–3]. A numerical investigation is presented in this work for a turbulent buoyant cavity flow at a relatively low Ra number, $Ra = 1.58 \times 10^9$. This makes a reasonable LES possible when using a computationally affordable grid resolution. It is expected that a detailed exploration of this type of flow will shed light on the flow physics and give some implications for further SGS modeling of turbulent buoyant flows. The simulation is compared with experimental data. The performance of the SGS model used is discussed, and the near-wall flow features are analyzed.

2. Simulation Methodology

2.1. The Subgrid Scale Models

The subgrid-scale stresses appearing in the filtered Navier-Stokes equations are responsible for the energy occurrence between the large-scale and the subgrid-scale eddies. They have often been modeled in alignment with the large-scale strain rate, $\bar{S}_{ij} = \frac{1}{2} \left(\frac{\partial \bar{u}_i}{\partial x_j} + \frac{\partial \bar{u}_j}{\partial x_i} \right)$, using the SGS

eddy viscosity, ν_t , i.e.,

$$\tau_{ij} = \overline{u_i u_j} - \bar{u}_i \bar{u}_j = -2\nu_t \bar{S}_{ij} + \frac{\delta_{ij}}{3} \tau_{kk}, \quad (1)$$

By means of the gradient diffusion hypothesis, the SGS heat fluxes, h_j , in the filtered thermal equation are modeled as

$$h_j = \overline{\theta u_j} - \bar{\theta} \bar{u}_j = -\alpha_t \frac{\partial \bar{\theta}}{\partial x_j}, \quad (2)$$

where $\alpha_t = \nu_t / Pr_t$ is the SGS diffusivity and Pr_t is the SGS Prandtl number.

The SGS viscosity is often formulated in terms of the filter width, Δ , and a time scaling quantity, \mathcal{T} , i.e. $\nu_t \propto \Delta^2 / \mathcal{T}$. In the well known Smagorinsky model, this time scaling is equal to the reciprocal of the magnitude of the resolved local strain rate tensor, $|\bar{S}| = \sqrt{2\bar{S}_{ij}\bar{S}_{ij}}$, giving $\nu_t = C\Delta^2 / \mathcal{T} = C\Delta^2 |\bar{S}|$. The SGS eddy diffusivity can then be written as $\alpha_t = C_t \Delta^2 / \mathcal{T} = (C\Delta^2 |\bar{S}|) / Pr_t$. For isothermal turbulent flows, this ν_t formulation suggests that a local equilibrium holds between the SGS shear production and the SGS dissipation rate. For natural convection flows where the buoyancy plays a significant role in the production, Eidson [4] proposed including the SGS buoyant production in the local equilibrium argument. As a result, the SGS time scaling takes the following form

$$\mathcal{T} = \left(|\bar{S}|^2 - \frac{g\beta}{Pr_t} \frac{\partial \bar{\theta}}{\partial x_j} \delta_{2j} \right)^{-\frac{1}{2}} \quad (3)$$

To avoid rendering non-real solutions from this scaling, it is often necessary to constrain the instantaneous SGS viscosity to be equal to zero as $|\bar{S}|^2 < \frac{g\beta}{Pr_t} \frac{\partial \bar{\theta}}{\partial x_j} \delta_{2j}$, particularly for solving thermally stratified flows. This constraint can be relaxed by using $|\bar{S}|$ to weight the Eidson time scaling, as done by Peng and Davidson [5]:

$$\mathcal{T} = \left(|\bar{S}| - \frac{g\beta}{Pr_t |\bar{S}|} \frac{\partial \bar{\theta}}{\partial x_j} \delta_{2j} \right)^{-1} \quad (4)$$

Nevertheless, the use of (4) requires a "clipping" in the total viscosity, $(\nu_t + \nu)$, which should not be negative to retain numerical stability. Unlike the Eidson model, the SGS viscosity computed from (4) allows negative values of ν_t in the range of $[0, -\nu]$. For isothermal flows, both (3) and (4) return to the conventional Smagorinsky time scaling.

Model coefficients, C and C_t , have been determined using the dynamic procedure [6, 7]. The SGS Prandtl number, Pr_t , can also be dynamically determined with different approaches as a function of time and space [5, 8]. In this work, we use $C = 0.0441$ and $Pr_t = 0.4$, as recommended by Eidson [4], when the base model with constant model coefficients is employed for comparison.

2.2. Numerical Method

The governing equations are discretized on a collocated grid using the second-order central differencing finite-volume method [9]. An implicit, fractional step method is used to solve the discretized equations constructed in a parallel code. The solution is advanced in time using the second-order Crank-Nicolson scheme. The filtered Navier-Stokes equation is discretized as follows

$$\bar{u}_i^{n+1} = \bar{u}_i^n + \Delta t H(\bar{u}_i^n, \bar{u}_i^{n+1}, \bar{b}_i^n) - \frac{1}{\rho} \alpha \Delta t \frac{\partial \bar{p}^{n+1}}{\partial x_i} - \frac{1}{\rho} (1 - \alpha) \Delta t \frac{\partial \bar{p}^n}{\partial x_i}, \quad (5)$$

where $\alpha = 0.5$, $H(\bar{u}_i^n, \bar{u}_i^{n+1}, \bar{b}_i^n)$ includes the convection, the viscous and SGS stresses and the buoyancy term, \bar{b}_i^n , in the gravitational direction. Equation (5) is solved with a symmetric Gauss-Seidel method. To reinforce the pressure-velocity coupling, an intermediate velocity field is computed by subtracting the implicit part of the pressure gradient from (5), giving

$$\bar{u}_i^* = \bar{u}_i^{n+1} + \frac{1}{\rho} \alpha \Delta t \frac{\partial \bar{p}^{n+1}}{\partial x_i}. \quad (6)$$

Taking the divergence of (6) leads to a Poisson equation for the pressure, i.e.,

$$\frac{\partial^2 \bar{p}^{n+1}}{\partial x_i \partial x_i} = \frac{\rho}{\alpha \Delta t} \frac{\partial \bar{u}_i^*}{\partial x_i}. \quad (7)$$

On the right-hand side of (7), the divergence of the velocity is computed from the velocities at the volume faces. The Poisson equation is solved using a multigrid method. The resultant pressure field, together with the intermediate velocities calculated from (6), is then used to correct the velocities at the volume faces. The filtered thermal energy equation is then solved, and SGS eddy viscosity is subsequently computed.

3. Results and Discussion

The natural convection was measured in an air-filled cavity with dimensions of $W = H = 0.5D$ in the x , y and z directions [10]. The isothermal vertical walls with a temperature difference of $\Delta\Theta = 40K$ are located at $x = 0$ and $x = W$, respectively. The Rayleigh number, $Ra = (g\beta\Delta\Theta H^3 Pr)/\nu^2$, is 1.58×10^9 . The flow was experimentally identified as being characterized by low turbulence, and no visible transition was detected in the boundary layer along the heated/cooled vertical walls. The bottom (at $y = 0$) and top (at $y = H$) walls are highly conducting boundaries. Through a well controlled experimental setup, it was claimed that the cavity offers two-dimensional flow in the middle of the spanwise direction ($z = D/2$) where the measurements had been made.

In the numerical computation, two types of boundary condition have been tested in the spanwise direction: using a homogeneous condition to approach a statistically two-dimensional simulation; and specifying an adiabatic wall condition to identify three-dimensional effects. A grid with $96 \times 96 \times 64$ meshes was used under both conditions. The grid is stretched near the wall in both the x and y directions, with 12–13 nodes clustered within $y^+ \leq 10$ near the vertical and horizontal walls. When a homogeneous flow is assumed in the spanwise direction, a uniform grid is employed and only half of the cavity depth ($D/2$) is taken. This will give a resolution of $\Delta z^+ \approx 32$ based on the wall friction velocity at the mid-height ($y = H/2$). Alternatively, a clustered near-wall grid is utilized when the wall condition is specified in this direction. The results shown below have been averaged with respect to time and the homogeneous direction (if any), denoted as $\langle \rangle$.

For all the simulations, it was found that the dynamic Smagorinsky model reproduces nearly identical results to those given by the dynamic modified buoyancy model, Eq. (4). It seems that the dynamic procedure is able to self-adjust the SGS viscosity to a similar level, or the strain term is generally less than the buoyancy term in (4) for the case considered. In the following comparison, the results of the dynamic model are based on the modified buoyancy model, using Eq. (4) for the SGS time scaling.

Fig. 1 shows the distributions of mean velocity and temperature at different locations, where the buoyant velocity $U_0 = \sqrt{g\beta\Delta\Theta H}$, the cold wall temperature, θ_{cw} , and $\Delta\Theta$ have been used

as normalization factors. The results computed with the dynamic model are for the homogeneous case in the spanwise direction. To reveal the effect of the spanwise grid resolution, the results obtained with a $96 \times 96 \times 32$ grid are also shown when using the same dynamic model, denoted with (z32) in the figure legend. The coarse grid reproduces a slightly narrow vertical boundary layer with a large velocity peak as compared with the experiment. Moreover, unlike the experimental observation that claims a stationary core region, the simulation produces weak circulation there. This is partly reflected by the wavy profile of the horizontal velocity along the vertical centerline (Fig. 1 c)). It will be further illustrated in Fig. 3 by visualizing the overall flow field.

For comparison, a group of results computed with the Smagorinsky model (Smag. model) for the case with no homogeneous direction (i.e. an adiabatic wall condition is assumed in the spanwise direction) is also presented in Fig 1. They have been taken from the $z = D/2$ plane without spatial averaging. It should be noted that the Smagorinsky model used here has been modified by multiplying a van Derist-type damping function, $f_\mu = (1 - \exp(y^+/25))^2$, to the model coefficient for a reasonable near-wall asymptotic behavior. The results computed by this model are generally worse than those given by the dynamic model. As the wall condition is specified at the spanwise boundaries, moreover, the antisymmetrical flow feature about the vertical centerplane will be somewhat altered. This can be seen in Fig. 1 c), which shows that the flow near the bottom wall has a larger magnitude of the horizontal velocity peak than that near the top wall out of which the backflow is however more intensive. In addition, it was found in this work that the flow at the mid-height is weaker near the hot wall in the mid-depth section ($z = D/2$) than in the side sections between the spanwise end wall and the $z = D/2$ plane, while it is stronger near the cold wall in the $z = D/2$ section.

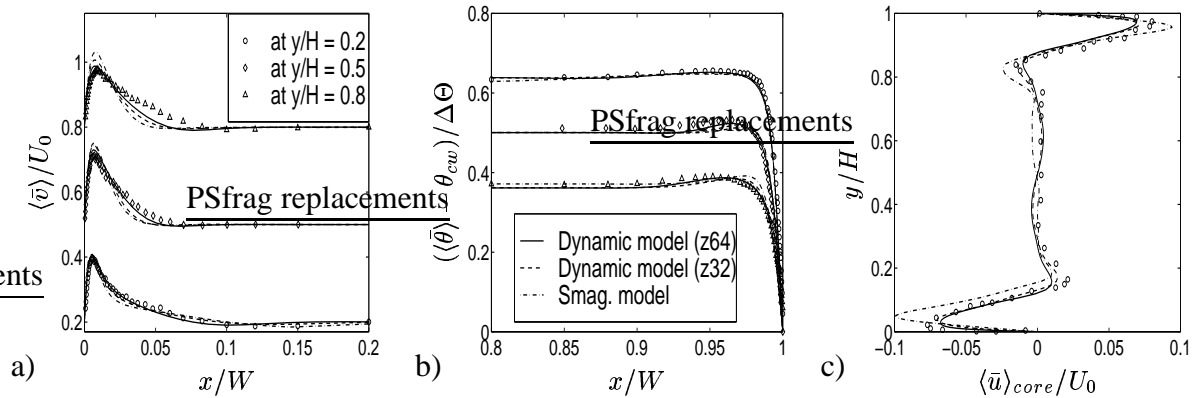


Figure 1: Comparison of predictions. a). Mean velocity near the hot wall; b). Mean temperature near the cold wall; c). Mean horizontal velocity at $x/W = 0.5$.

In Fig. 2, the local Nusselt number, $Nu_l = -(H\partial\langle\bar{\theta}\rangle/\partial n|_w)/\Delta\Theta$, and the wall friction coefficient, $C_f = \langle\tau_w\rangle/(\rho U_0^2/2)$, are compared with the experimental data. No experimental data are available for C_f along the top and bottom walls. On the lower part of the vertical walls, the simulation yields lower heat transfer and larger wall friction than the experiment. In general, the dynamic model with fine numerical resolution in the spanwise direction yields more satisfactory results than are given with the coarse resolution and by the Smagorinsky model as compared with the experimental data.

Fig. 3 illustrates the streamtraces and the isothermal lines for the case with a homogeneous spanwise flow, which is taken as the only case presented in the following. The simulation shows

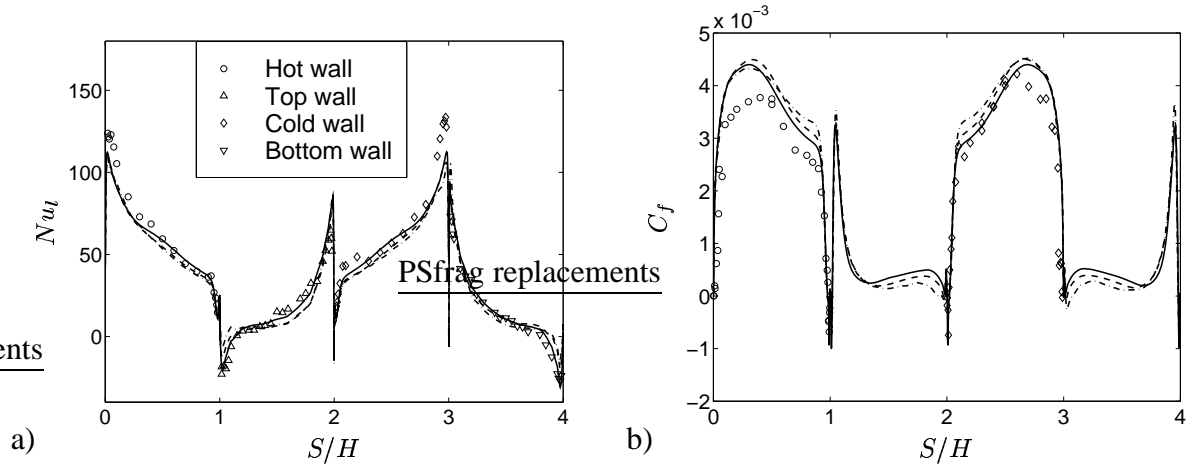


Figure 2: Predictions of wall parameters (starting from the lower left-hand corner along the cavity closure surface (S) clockwise, same legend for the lines as in Fig. 1). a). Local Nusselt number; b). Wall friction coefficient.

good antisymmetric flow feature, even with the tiny bubbles in the upper left-hand corner and lower right-hand corner. There is no bubble predicted in the other two corners. There exist several recirculation regions away from the wall boundary layer flows. The bubbles neighboring the wall flows are comparatively strong. With increasing Rayleigh numbers, the boundary layer flow may be more intensive, the recirculation bubbles are expected to merge with each other to form a large recirculating motion around the core region.

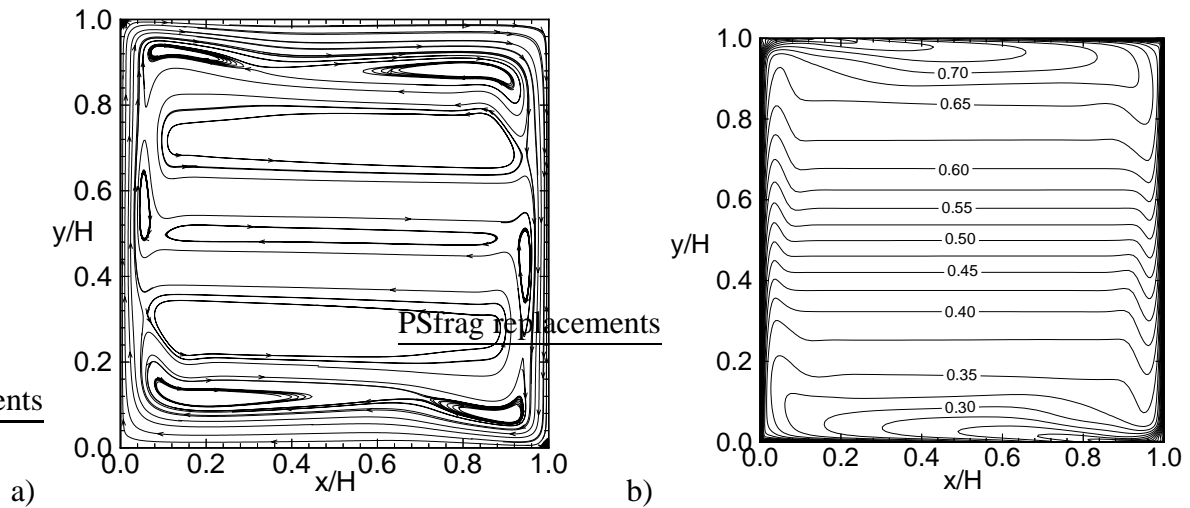


Figure 3: Illustrations of the flow and thermal fields. a). Flow streamlines; b). Isothermal lines, normalized as $(\langle \bar{\theta} \rangle - \theta_{cw}) / \Delta\Theta$.

Fig. 4 plots the distributions for the turbulence statistics, for which the fluctuation of a variable has been computed from $\phi' = \bar{\phi} - \langle \bar{\phi} \rangle$. Comparing to the mean flow predictions, in general, these computed statistics show a relatively large discrepancy in comparison with the measured data. The velocity fluctuation in the streamwise direction of the boundary layer agrees however reasonably well with the experiment. The level of the horizontal velocity fluctuation, $\sqrt{\langle u'^2 \rangle}$, is overall underpredicted compared with the experiment. It seems that an appreciable fraction

of this component might reside in the subgrid-scale motions. In the outer shear layer between the near-wall flow and the core region, the velocity statistics are generally underpredicted while the thermal fluctuation is overpredicted. It suggests that an adequate modeling of the flow in this outer layer is as important as of that in the vicinity of the wall. Fig. 4 d) and e) plot the total Reynolds shear stress and horizontal heat flux at location $y = 0.5H$ (dotted line). The SGS part is significantly smaller than its resolvable counterpart. The visible SGS contribution is not in the vicinity of the wall but in regions immediately neighboring or in the outer part of the boundary layer.

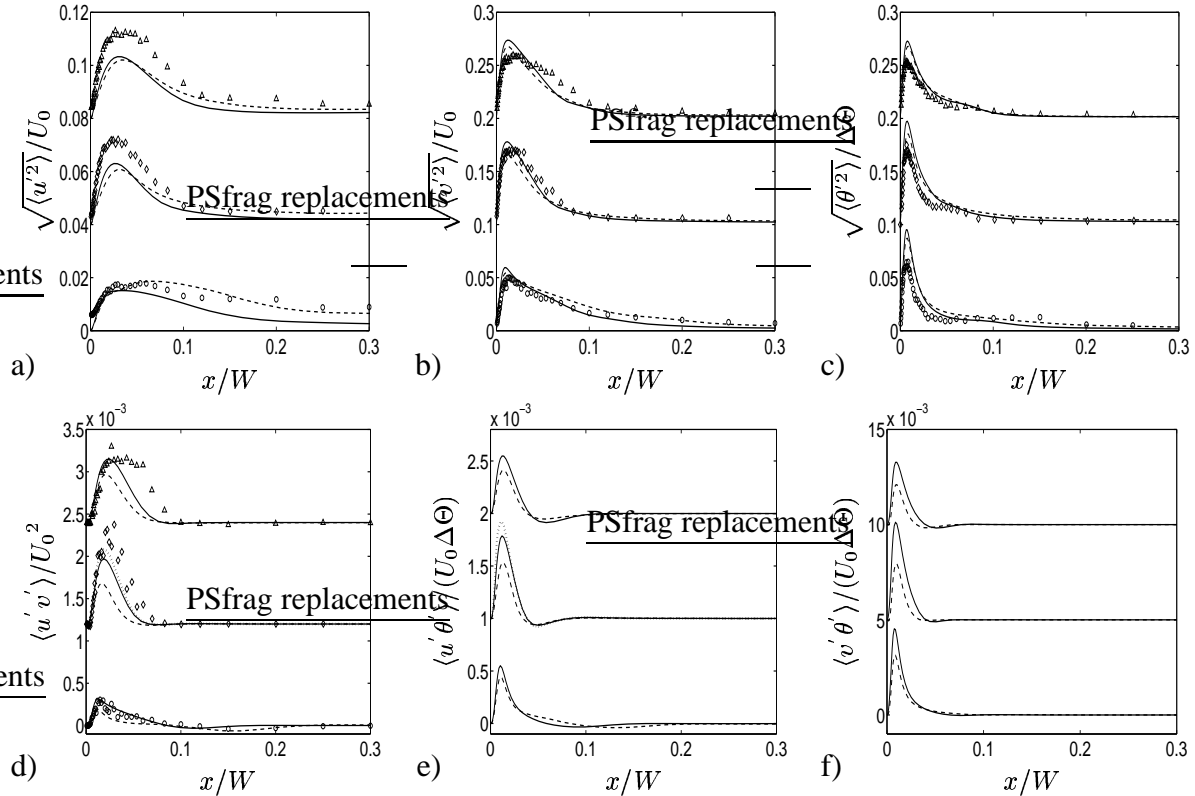


Figure 4: Predictions of turbulence statistics with the dynamic model at $y/H = 0.2, 0.5$ and 0.8 from bottom to top. Solid line is with the $96 \times 96 \times 64$ grid (z64), dashed line with the $96 \times 96 \times 32$ grid (z32). In d) and e) the dotted line at $y/H = 0.5$ represents the total Reynolds shear stress and heat flux.

At the mid-height ($y = H/2$) the linear viscous sublayer in the vertical boundary layer is approximately within $x^+ < 3.5$. Fig. 5 a) shows the detailed flow structure in the viscous/conductive sublayer close to the hot wall (at $x^+ = 2$) by plotting the contours of instantaneous v' and spanwise vorticity, $\omega_z' = (\partial v'/\partial x - \partial u'/\partial y)$, for which the positive values are contoured by solid lines and negative values by dashed lines. The flow seems to have a tendency to exhibit some coherent structures similar to those in a forced convection boundary layer, but they are not as elongated. In Fig. 5 a), the structure of high-speed ($v' > 0$) and low-speed ($v' < 0$) streaks emerge alternately in the spanwise direction above $y/H \approx 0.3$ (indicated by high concentration contour lines). Away from the wall, e.g. at $x^+ = 5.25$, they are absent (not shown here). Fig. 5 b) shows the corresponding contour of ω_z' . The regions with large positive values of ω_z' are associated with the regions consisting of high-speed streaks.

The coherent structure disappears in the vicinity of the horizontal top wall as shown in Fig. 6 on a x - z plane at $y^+ = 0.5$ close to the top wall. Near the hot wall (on the left-hand side), a

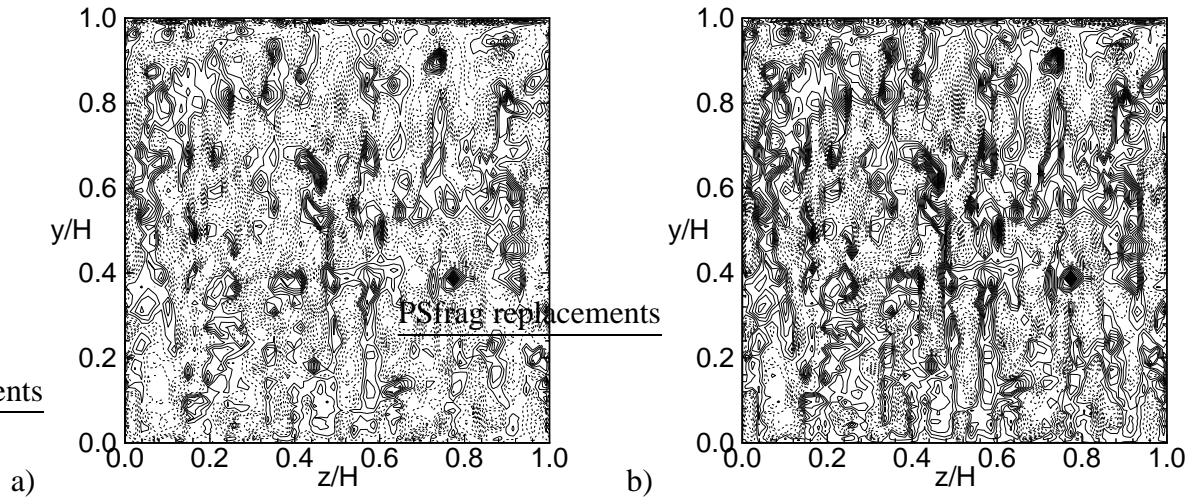


Figure 5: Contour of v' and ω_z' at a y - z plane near the hot wall (at $x^+ = 2$ based on the wall friction velocity at $y = H/2$, with $96 \times 96 \times 64$ grid resolution). a). Contour of v' ; b). Contour of ω_z' .

narrow region with large values of u' exists owing to the vertical boundary layer fbw impinging on the top wall (Fig. 6 a)). The excess momentum in this fbw is however quickly exhausted, and the fbw tends to be relaminarized. Without showing an illustration here, moreover, it was found in the simulation that energy backscatter occurs (detected by negative ν_t) in the lower left and upper right corners where the vertical boundary layer fbw starts. In these small regions, even the time-averaged SGS viscosity retains negative values. It implies that the local fbw constantly undergoes a net energy transfer from the subgrid scales to the resolvable scales.

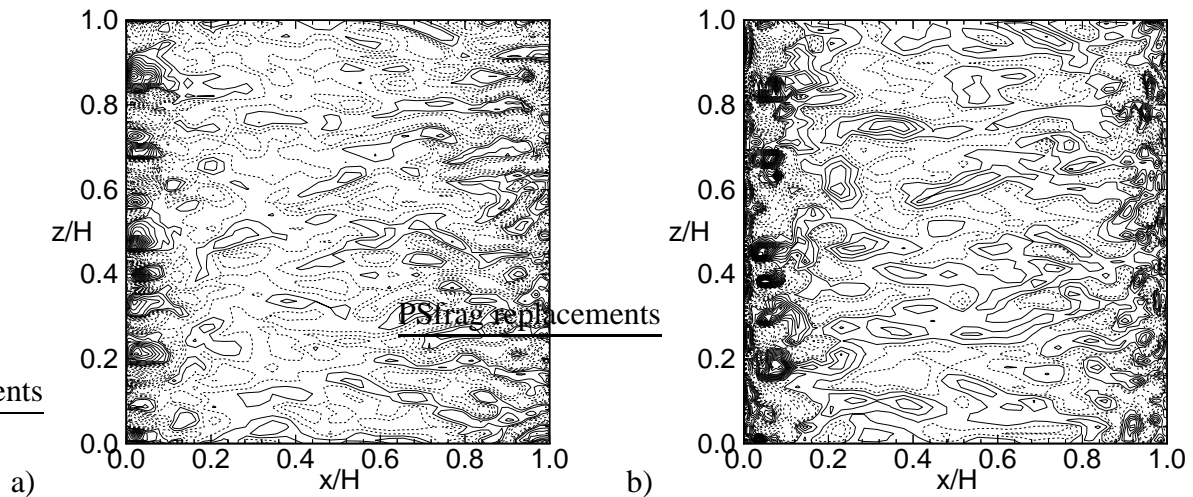


Figure 6: Contour of u' and ω_z' at a x - z plane near the top wall (at $y^+ = 0.5$ based on the wall friction velocity at $x = W/2$, with $96 \times 96 \times 64$ grid resolution). a). Contour of u' ; b). Contour of ω_z' .

4. Conclusions

A turbulent buoyant fbw in a side-wall heated cavity was studied using LES techniques. The fbw is characterized by low turbulence level and thermal stratification. In general, the Smagorinsky model (without being incorporated into the dynamic procedure) reproduces results in

larger discrepancies than does the modified dynamic model as compared with the experimental data. This is particularly the case in the shear layer between the wall flow and the cavity core region. The dynamic model is able to yield mean flow quantities that are in rather good agreement with the measured data, but less accurate for some turbulence statistics.

The discrepancies between the experimental data and the computed results in the outer part of the near-wall boundary layer suggest that special attention should be paid to the flow physics and numerical treatment in this region. Moreover, it was demonstrated that the numerical resolution in the homogeneous direction is of importance for better predictions as well as for reasonable resolution of near-wall flow structures. Similar to the forced convection boundary layer, the natural convection flow along the heated/cooled cavity walls tends to exhibit coherent structures with low- and high-speed streaks, but the size is relatively small at low Rayleigh numbers as such considered in this work. In the boundary layer near the horizontal wall, no such structures are detected however, where the flow instead tends to be relaminarized.

Acknowledgements

The authors are grateful to Dr. Y. S. Tian for providing the experimental data.

References

1. R. A. W. M. Henkes and C. J. Hoogendoorn. Comparison exercise for computations of turbulent natural convection in enclosures. *Numerical Heat Transfer, Part B*, 28:59–78, 1995.
2. S.-H. Peng and L. Davidson. Computation of turbulent buoyant flows in enclosures with low-Reynolds-number $k - \omega$ models. *Int. J. Heat and Fluid Flow*, 20:172–184, 1999.
3. S.-H. Peng and L. Davidson. Large eddy simulation for turbulent buoyant flows induced by differentially heated vertical walls. Report 98/8, Department of Thermo and Fluid Dynamics, Chalmers University of Technology, Gothenburg, 1998.
4. T.M. Eidson. Numerical simulation of the turbulent Rayleigh-Bénard problem using subgrid modelling. *J. Fluid Mech.*, 158:245–268, 1985.
5. S.-H. Peng and L. Davidson. Comparison of subgrid-scale models in LES for turbulent convection flow with heat transfer. In *2nd EF Conference in Turbulent Heat Transfer*, pages 5.24–5.35. Manchester, UK, 1998.
6. M. Germano, U. Piomelli, P. Moin, and W.H. Cabot. A dynamic subgrid-scale eddy viscosity model. *Phys. Fluids A*, 3:1760–1765, 1991.
7. W. Cabot and P. Moin. Large-eddy simulations of scalar transport with the dynamic subgrid-scale model. In B. Galperin and S.A. Orzag, editors, *Large Eddy Simulation of Complex Engineering and Geophysical Flows*, pages 141–158, New York, 1993. Cambridge University Press.
8. W. Cabot. Large-eddy simulations of time-dependent and buoyancy-driven channel flows. In *Annual Research Briefs 1992*, pages 45–60, Center for Turbulent Research, Stanford Univ./NASA Ames Research Center, 1992.
9. L. Davidson. LES of recirculating flow without any homogeneous direction: A dynamic one-equation subgrid model. In *2nd Int. Symp. on Turbulence Heat and Mass Transfer*, pages 481–490, Delft, 1997.
10. Y. S. Tian. *Low Turbulence Natural Convection in an Air Filled Square Cavity*. PhD thesis, South Bank University, London, UK, 1997.